HHS Public Access

Author manuscript

Mitochondrion. Author manuscript; available in PMC 2021 May 01.

Published in final edited form as:

Mitochondrion. 2020 May ; 52: 8–19. doi:10.1016/j.mito.2020.02.002.

Prophylaxis of Mitochondrial Dysfunction Caused by Cellular Decompression from Hyperbaric Exposure

Abhay Ranganathan[1], **Shawn Owiredu**[2], **David H. Jang**[2], **David M. Eckmann**[1,3]

[1]Department of Anesthesiology and Critical Care, Perelman School of Medicine, University of Pennsylvania, Philadelphia, PA 19104

[2]Department of Emergency Medicine, Perelman School of Medicine, University of Pennsylvania, Philadelphia, PA 19104

[3]Department of Bioengineering, School of Engineering and Applied Sciences, University of Pennsylvania, Philadelphia, PA 19104

Abstract

Mitochondrial dysfunction occurring in response to cellular perturbations can include altered mitochondrial motility and bioenergetic function having intracellular heterogeneity. Exogenous mitochondrial directed therapy may correct these dysfunctions. Using *in vitro* approaches, we find that cell perturbations induced by rapid decompression from hyperbaric conditions with specific gas exposures has differential effects on mitochondrial motility, inner membrane potential, cellular respiration, reactive oxygen species production, impaired maintenance of cell shape and altered intracellular distribution of bioenergetic capacity in perinuclear and cell peripheral domains. Addition of a first-generation cell-permeable succinate prodrug to support mitochondrial function has positive overall effects in blunting the resultant bioenergy responses. Our results with this model of perturbed cell function induced by rapid decompression indicate that alterations in bioenergetic state are partitioned within the cell, as directly assessed by a combination of mitochondrial respiration and dynamics measurements. Reductions in the observed level of dysfunction produced can be achieved with application of the cell-permeable succinate prodrug.

Keywords

bioenergetics; decompression; intermembrane potential; microscopy; mitochondria; motility; perinuclear; respiration

Address for Correspondence: David M. Eckmann, PhD, MD, N429 Doan Hall, 410 W 10th Ave, Columbus OH 43210, 614.685.8274 Office, david.eckmann@osumc.edu.

6. **Declarations of interest:** none.

1. Introduction

Mitochondrial dysfunction is a recognized as an important contributor to the pathogenesis of many health disorders, including cardiomyopathy, coronary artery disease, skeletal muscle atrophy, chronic fatigue syndrome, dementia and Alzheimer's disease, diabetes, and psychiatric disorders (Galvan et al., 2017; Kim et al., 2019; Wilkins and Swerdlow, 2016), and generally reflects the presence of cellular stress. The bioenergetic demands on cells can exceed their intrinsic bioenergetic capacity under stress, disease or injury conditions, thus rendering cells unable to meet all of their bioenergy requirements. In such circumstances, this can disrupt energy-dependent functions occurring in the cell periphery or within the cell nucleus and can manifest as alterations in mitochondrial dynamics involving mitochondrial motility and other functions (Kandel et al., 2015), as changes in mitochondrial respiratory function (Kandel et al., 2016), or even as disturbances in both mitochondrial dynamic and respiratory functions (Jang et al., 2017c). For instance, both select medications (Gorini et al., 2018; Guigni et al., 2018; Kucera et al., 2017; Lin et al., 2019; Porporato et al., 2018; Ramachandran and Wierzbicki, 2017) and environmental toxicants (Lee et al., 2010; Meyer et al., 2013) have been demonstrated to alter mitochondrial dynamic and respiratory functions. These may include changes in mitochondrial motility, perinuclear clustering and size, and may also impair bioenergetics functions including respiratory chain performance, maintenance of intermembrane potential and rates of production of reactive oxygen species (Jang et al., 2019a; Jang et al., 2018b; Jang et al., 2019b). Cumulatively, these effects lead to intracellular partitioning of bioenergy delivery to the cell nucleus and the cell periphery that can detrimentally impact cell health (Eckmann et al., 2019).

Overall such findings suggest that common signaling mechanisms are involved in the cellular response to perturbations such as injury or illness which culminate in the development of impaired mitochondrial respiration, altered mitochondrial dynamics and reduced bioenergy delivery to particular regions of the cell (Chandel, 2014; Kotiadis et al., 2014; Whelan and Zuckerbraun, 2013). This also suggests that targets for mitochondrial-directed therapy exist and that the associated biological mechanisms can potentially be exploited to protect cells from degradation of necessary bioenergy functions despite the presence of conditions that challenge metabolic capabilities (Distelmaier et al., 2017; Ehinger et al., 2016; Piel et al., 2018). These targets include Complex II (CII) via the use of cell-permeable succinate prodrugs such as diacetoxy-methyl succinate (NV118) which can access mitochondria and bypass Complex I (CI) (Ehinger et al., 2016).

Conditions that have been proven to alter both mitochondrial respiration and mitochondrial dynamics include rapid decompression from hyperbaric exposure (Jang et al., 2018c). In that work we rapidly decompressed human dermal fibroblast cells from hyperbaric exposure to air, nitrogen and oxygen as can occur in recreational or occupational underwater diving. We performed high-resolution respirometry (HRR) to examine key respiratory states following decompression from hyperbaric exposures and we coupled our findings to parallel fluorescence microscopy imaging-based measurements of mitochondrial dynamic function, including net mitochondrial movement, number, and size. Key findings were that maximal respiration and cellular bioenergetic reserve were gas mixture exposure dependent, as was any decrement in mitochondrial motility, when compared to baseline. Decompression from

hyperbaric oxygen and air exposures produced deleterious effects on overall mitochondrial function, with cytoskeletal imaging providing additional evidence of associated alterations in cell morphology. An important implication of this study is the potential for exogenous compounds to provide prophylaxis and blunt the degree of impairment in these measures of mitochondrial function and cell morphology that are otherwise induced by the applied hyperbaric exposures and subsequent decompression (Distelmaier et al., 2017; Ehinger et al., 2016; Piel et al., 2018).

We now utilize these and additional methodologies, including measurement of intermembrane potential, superoxide production, and cell morphology, to evaluate mitochondrial and cellular responses (Kandel et al., 2015; Kandel et al., 2017) to decompression from hyperbaric conditions as they occur in a previously untested yet relevant cell line, human aortic smooth muscle cells (HAoSMCs). An important new approach undertaken in this work is to investigate the intracellular compartmentalization of mitochondrial dynamics in cell peripheral and perinuclear domains, as has already been performed to examine mitochondrial responses to liquid anesthetic exposure (Eckmann et al., 2019). Additionally, perinuclear clustering of mitochondria has been observed in cells under distressed conditions (Dzeja et al., 2002). Based on these details, herein we apply our established methodology to partition the cell interior into both peripheral and perinuclear zones (Eckmann et al., 2019) as shown in Figure 1A. We do this in order to assess intracellular inhomogeneities of mitochondrial dynamics, to evaluate the compartmentalization of bioenergy distribution within the HAoSMCs under the various experimental conditions and to examine other measureable effects of decompression from hyperbaric conditions. We also use this approach to quantify the degree of prophylaxis from those measurable effects provided by the exogenous compound. Figure 1B-E recapitulates our methodology (Eckmann et al., 2019) for creation of a mask for image analysis that enables partitioning the cell into both perinuclear and peripheral zones, as described in the Methods section. Employing this technique facilitates the assessment of mitochondrial responses within each specified intracellular domain. The domain size we establish for the perinuclear region, as described in the Methods Section, is based on the intracellular diffusion coefficient of ATP and the associated diffusion time (Hubley et al., 1995), which yields a diffusion length scale for ATP of ~ 3 μm. This is entirely consistent with the distance measured between the cell nucleus and mitochondria that have clustered around it (Dzeja et al., 2002). It also fulfills the need to minimize the distance that ATP molecules must travel by diffusion to reach the cell nucleus, which lacks mitochondria of its own.

Herein we also demonstrate effects of a cell-permeable succinate prodrug, NV118 (Ehinger et al., 2016; Piel et al., 2018), to mitigate in part the mitochondrial responses to the imposed environmental conditions and, thus prophylactically maintain bioenergy availability within cells that otherwise would demonstrate greater bioenergy perturbations. We first establish baseline mitochondrial dynamics and bioenergetics *in vitro* and quantify alterations of mitochondrial dynamics and bioenergetics induced by rapid decompression from select hyperbaric gas exposure conditions. We then assess effects of the cell-permeable succinate prodrug to decrease the decrement in mitochondrial dysfunction otherwise caused by the decompression from hyperbaric conditions. This preclinical study includes both cell perturbation effects on partitioning of intracellular bioenergy availability and efficacy of a

potential prophylaxis strategy to preserve cell bioenergy functions, thus providing a framework for additional *in vitro* and vivo experiments involving other sources of cell bioenergy perturbation.

2. Results

2.1 Alterations in mitochondrial potential and motility that follow decompression from hyperbaric exposures are partially preserved with cell-permeable succinate prodrug NV118.

Using HAoSMCs we first assessed the influences of rapid decompression from hyperbaric exposure on mitochondrial inner membrane potential (Eckmann et al., 2019) and mitochondrial motility (Jang et al., 2018c). We also assessed the impact of NV118, added to cells in advance of the decompression event, on mitigation of any changes in membrane potential or mitochondrial motility otherwise induced by the combination of hyperbaric exposure plus rapid decompression. The applied cellular perturbations included decompression from hyperbaric exposure to air (Figure 2), nitrogen (Figure 3) and oxygen (Figure 4). These perturbations were not sufficient to increase cell death rates from baseline, as indicated by cell viability studies conducted with trypan blue (0.4%) exclusion staining. The membrane potential imaging demonstrates fluorescence that is brighter in a thin perinuclear region than in the cell periphery at baseline (Figures 2A, 3A, 4A), following decompression from any of the hyperbaric exposure conditions (Figures 2B, 3B, 4B), as well as following decompression but with NV118 present (Figures 2C, 3C, 4C). These microscopy images are not presented at the same image intensity due to the very wide range of brightness between images. Within each image, however, the range of brightness does exceed the lower thresholding limit for imaging mitochondria without incurring saturation effects (Kandel et al., 2015). While these large differences which arise between experimental conditions do prevent direct visual comparisons between the different images shown (direct comparisons from advanced quantitative image analysis are indicated separately below), direct visual comparison between mitochondria in the perinuclear and peripheral regions of the cell can be made within a single frame. This does discernibly show the presence of differences in membrane potential between these two regions for base conditions, following decompression from hyperbaric air exposure with NV118 added (Figure 2C), and following decompression from hyperbaric oxygen exposure both without (Figure 4B) and with NV118 utilized (Figure 4C).

We also used our mitochondrial imaging to create heat maps of individual mitochondrial motility (Jang et al., 2018c; Jang et al., 2017c; Kandel et al., 2015). Each dot on the heat maps represents a distinct mitochondrion in its final location within the microscopy plane after tracking. Each dot's color is a representation of its measured motility, assessed as the log of the net distance traveled according to an accompanying color scale. The images demonstrate a shift from the cooler colors (e.g., blue/white, indicating a smaller degree of individual net mitochondrial movement) at baseline conditions (Figures 2D, 3D, 4D) toward the hotter colors (e.g., white/red, indicating greater individual mitochondrial movement) after decompression from hyperbaric conditions (Figures 2E, 3E, 4E). The addition of NV118 prior to the decompression event shifted the individual mitochondrial motility back

into the blue/white domain for each of the decompressions from hyperbaric conditions (Figures 2F, 3F, 4F).

The net distances traveled by mitochondria follow a log-normal distribution (Barel et al., 2017; Eckmann et al., 2019; Jang et al., 2018c; Kandel et al., 2015), and this occurs in both the cell periphery and in the perinuclear region. In both these regions, the log-normal distributions are shifted rightward (increased mitochondrial movement) in comparison to baseline following decompression from hyperbaric exposure to air (Figures 2G, 2H), nitrogen (Figures 3G, 3H) and oxygen (Figures 4G, 4H). However, in those cases in which NV118 was added to cells just prior to the hyperbaric exposure and subsequent decompression, the resultant mitochondrial motility was shifted leftward to a degree that at least matched motility at baseline conditions (e.g., perinuclear zone, oxygen exposure, Figure 4G), or actually left-shifted in comparison to baseline (Figures 2G-H, 3G-H, 4H). In all cases, the rightward distribution shifts following decompression from hyperbaric exposure, as compared to baseline, indicated a marked increase in mitochondrial motility, whereas all the leftward log normal distribution shifts evident in comparing decompression from hyperbaric exposure with NV118 present to cases without it, indicated a marked decrease in mitochondrial motility. Because the measurement of mitochondrial motility does not adhere to a linear Gaussian distribution, the mean value of the motion and its standard deviation does not yield an appropriate parameter for statistical comparison. Instead, the geometric mean is selected to represent the central tendency of the net distances traveled by mitochondria to follow a log-normal distribution. The specific values of the geometric means of the mitochondrial net distances traveled (measured in nm) appear in Table 1 for each of the decompression from hyperbaric exposure conditions, as do the resultant P values for statistical comparisons between the groups (Eckmann et al., 2019; Jang et al., 2017c; Kandel et al., 2015). These comparisons show that mitochondrial motility is significantly increased in both the perinuclear region and the cell periphery for each of the decompression from hyperbaric exposure conditions compared with baseline conditions and that the addition of NV118 mitigates the increase in motility induced by decompression from hyperbaric conditions.

The aforementioned results suggest that there exist intracellular distinctions and inhomogeneities in mitochondrial motility and, potentially, in mitochondrial respiration. These result from the different gas compositions used in the compression/decompression exposure as well as from the cell-permeable succinate prodrug delivered. This prompted us to explore further the key cellular respiration parameters (Jang et al., 2017a; Jang et al., 2017b) as well as additional measures of mitochondrial dynamics affecting the HAoSMCs undergoing environmental exposure to perturb cells.

2.2 Key cellular respiration parameters are sensitive to decompression and cell-permeable succinate prodrug NV118.

Previously we showed that decompression of human dermal fibroblasts from hyperbaric conditions resulted in decreased basal and maximum respiration with oxygen exposure, decreased maximum respiration following air exposure and increased leak following nitrogen exposure (Jang et al., 2018c). The data in our present study suggest that the effects

of decompression from hyperbaric conditions on cellular respiration are dependent on cell-type. The data also indicate that the respiration is responsive to addition of the succinate compound. Consistent with this view are the measurements of basal respiration (Figure 5A), which demonstrates that the oxygen consumption rate for ATP-linked respiration is exposure-dependent and can either increase or decrease from baseline values, depending on the exposure. Key findings include an increase in basal respiration following decompression from hyperbaric air exposure, whereas it decreased following decompression from hyperbaric oxygen exposure. In both cases, the application of NV118 yielded a further increase in basal respiration. Maximal respiration (Figure 5B) decreased following decompression from both hyperbaric air and oxygen exposure, and it further decreased in the oxygen exposure group with NV118 provided. The cumulative effect of these two measures is shown in the spare respiratory capacity, or SRC (Figure 5C), which is decreased in all decompression from hyperbaric exposure conditions compared to baseline, further decreased in the air and oxygen exposure groups with NV118 given, but increased above baseline in the nitrogen exposure group having received NV118.

The superoxide production obtained with MitoSOX, displayed as the average corrected total cell fluorescence (CTCF) in Figure 5D, indicates an increase following decompression from both hyperbaric air and oxygen exposure compared to baseline, whereas it is decreased following decompression from hyperbaric nitrogen exposure. The addition of NV118 reduces superoxide production below baseline values for the air and oxygen exposures. With NV118 added to cells undergoing decompression from hyperbaric nitrogen exposure, the superoxide production is no different from baseline.

2.3 Intracellular mitochondrial partitioning reveals application of cell-permeable succinate prodrug NV118 preserves nuclear bioenergetics.

Our findings above indicate that mitochondrial motility and inner membrane potential are not equal in the region near the cell nucleus and in the cell periphery. As indicated above and illustrated in Figure 1A, we partitioned the intracellular space into both peripheral and perinuclear zones (Eckmann et al., 2019). Mitochondrial length (Kandel et al., 2015) was measured to be equal in the two zones at baseline (Figure 6A), but mitochondria are shorter within the perinuclear zone compared to the cell periphery following decompression from hyperbaric air exposure (with and without NV118) and following decompression from the hyperbaric nitrogen exposure. Figure 6A also demonstrates that mitochondria are shorter in the perinuclear zone compared to baseline for decompression from hyperbaric air and nitrogen exposures, while they are longer compared to baseline for decompression from hyperbaric oxygen exposure. Addition of NV118 results in preservation of these mitochondrial lengths so they are not different from baseline. There are no differences in mitochondrial length in the peripheral zone between baseline and any of the experimental conditions.

Figure 6B presents the mitochondrial inner membrane potential determined from TMRM average fluorescence intensity ratios for decompression from all hyperbaric exposure conditions in both the perinuclear and peripheral regions of the cells with and without pretreatment of NV118 (Eckmann et al., 2019) as well as controls for cells exposed to

carbonyl cyanide p-trifluoro-methoxyphenyl hydrazone (CCCP) at baseline. These are the quantitative data that accompany the imaging for which individual examples appear as Figures 2A-C, 3A-C and 4A-C. The data are normalized by the mean value for the measurement in the perinuclear zone under baseline conditions (see Methods below). These data demonstrate multiple features. There was a significant difference in the TMRM intensity ratio for the perinuclear area within the group undergoing decompression from hyperbaric oxygen exposure and having been provided NV118. For the peripheral region, there was a significant difference with NV118 pretreatment for decompression from both hyperbaric air and oxygen exposure. With the exception of the nitrogen exposure, the potential is lower in periphery than in the perinuclear zone. The potential in the perinuclear zone is lower under all conditions compared to baseline. Except for decompression from hyperbaric air exposure with NV118, the potential in the peripheral zone is always lower than that at baseline. With the exception of the cell periphery in the group undergoing decompression following hyperbaric nitrogen exposure, the potential is increased following addition of NV118.

The calculated values of the scaled fractional ATP-linked respiration (Figure 6C) are determined from the volumetric intracellular partitioning of the mitochondria between the perinuclear and cell peripheral regions, the respective values for mitochondrial potentials, and the measured respiration rates, including basal and leak (Eckmann et al., 2019). The graph is scaled to the mean value for baseline and demonstrates the increase in overall ATP-linked respiration with NV118 pretreatment for a particular experimental condition. Of note, this effect is the result of bioenergy activity occurring primarily in the cell periphery, as there is essentially no difference in the perinuclear component of ATP-linked respiration resulting from the addition of NV118 for decompression from a specific hyperbaric exposure condition. Additionally, the magnitude of the perinuclear component of ATP-linked respiration remains well preserved across all the experimental conditions with the exception of the oxygen exposures, for which it is slightly decreased both with and without NV118.

One functional measure of cellular response to perturbation is the ability of cells to maintain their shape. This depends on many factors, including cytoskeletal integrity (Kandel et al., 2017) and is an energy dependent process linked to ATP availability (Rangamani et al., 2014). Imaging of cell cytoskeleton, including actin and microtubules, was used to interrogate cytostructural features of HAoSMCs under baseline conditions, and following decompression from hyperbaric exposure to air, nitrogen and oxygen with and without NV118 included. As shown in Figure 6D, which presents results for cell circularity, cell shape did appear to depend on environmental exposure. We measured the circularity of cells following established methodology to define the cell outline, determine cell perimeter and cross sectional area from the imaging (Kandel et al., 2017). Examples of the cell imaging used for this analysis appear in Figure 6E-K, which shows cell filamentous organization on the left side of each image and the accompanying cell outline on the right side for the different experimental exposures. Following decompression from each type of hyperbaric gas exposure there is a significant increase in the mean value of the circularity parameter and a large variance compared to baseline (Figure 6D). This indicates a loss of maintenance of cell shape resulting from the decompression from the respective hyperbaric exposure. For each condition of decompression from hyperbaric exposure, the addition of NV118 results in

lesser perturbation in mean value of the circularity parameter as well as a decrease in the variance. This indicates that the inclusion of the exogenous compound better enables cells to maintain their shape in the face of decompression from the hyperbaric exposure.

3. Discussion

In this study we have measured changes in mitochondrial function, including mitochondrial dynamics and cellular respiration parameters, occurring in response to an applied environmental cellular perturbation. We have shown that this environmental challenge leads to an increase in metabolic demand that is dependent on features of the applied perturbation (e.g., specific gas composition to which cells are exposed during the compression/decompression cycle). We have further demonstrated for the first time that the changes induced by these conditions, including alterations in mitochondrial motility and effects on cell morphology, are mitigated in part by the administration of the cell-permeable succinate prodrug NV118. The cell line we have used, HAoSMCs, has been used to study vascular wound healing, tissue remodeling, and vascular differentiation relevant to diving and hyperbaric oxygen treatment (Mazur et al., 2016). Here we demonstrated differential alterations in both mitochondrial respiratory and dynamic motility function resulting from decompression from hyperbaric exposure. Similar to our previous study with fibroblasts, the gas mixture used was different between groups while the other related variables including absolute pressure exposure, hyperbaric compression and decompression rate, temperature, and cell type were all held constant (Jang et al., 2018c). As a new study using additional image analysis methods to partition cells into perinuclear and peripheral regions, we employed a more comprehensive examination of zone-based mitochondrial function. This was motivated by our consideration that the perinuclear clustering of mitochondria serves to minimize the distance that ATP molecules must diffuse to satisfy the nucleus' energy needs (Jang et al., 2019a). It is already established that the intracellular diffusion coefficient of ATP is in the range of $2.5 \pm 0.3 \times 10^{-6}$ cm^2/s, with a diffusion time of approximately 19 ms (Hubley et al., 1995). This yields a diffusion length scale for ATP in cells that is in the range of 3 μm, which is a length scale that is consistent with the extent of the region determined by microscopy methodology to represent the thickness of the perinuclear zone in which mitochondria cluster around the cell nucleus (Dzeja et al., 2002). We also evaluated the *in vitro* application of the cell-permeable succinate prodrug NV118 (Ehinger et al., 2016) to investigate mitigation of the mitochondrial dysfunction imposed by these injurious, but non-fatal decompression exposure conditions.

We measured changes in mitochondrial respiration specially looking at how both ATP-linked respiration and SRC in response to the cellular perturbations imposed by the decompression from hyperbaric exposure conditions. ATP-linked respiration reflects the oxygen consumption related to Complex V in the generation of ATP. In our analysis we found that cells exposed to hyperbaric oxygen demonstrated lower ATP-linked respiration compared to all other groups. This was consistent with our previous work in which we also demonstrated both lower basal respiration and maximal respiration in fibroblasts exposed to hyperbaric oxygen (Jang et al., 2019b). One study illustrated increased reactive oxygen species (ROS) is related to a higher oxygen partial pressure which likely reflects oxygen toxicity due to hyperoxia (Wang et al., 2015). In this work we also demonstrated significantly higher

superoxide production measured as MitoSOX in the Oxygen group when compared to the baseline group which further supports the detrimental effect of excessive ROS.

We examined the SRC in all groups. SRC is used to describe the additional production of ATP that can occur in the event of a sudden increase in energy demand. Depletion of the SRC has been shown to relate to a range of pathologies affecting high energy requiring tissues such as the heart and brain, both of which are particularly susceptible to decompression exposure (Leitch and Hallenbeck, 1985; Vann et al., 2011). In our study, the air, nitrogen, and oxygen groups all demonstrated lower SRC which likely reflects the increase in cellular demand from the perturbations induced by the decompression from hyperbaric exposure conditions (Chacko et al., 2014). As seen in Figure 5D, the superoxide production was significantly higher in the air and oxygen groups when compared to baseline, which likely reflects the importance of ROS in this process. There were no changes in ATP-linked respiration in the nitrogen group, as also occurred with fibroblasts in our previous study (Jang et al., 2018c). This is likely due to nitrogen having minimal or no effect on induction of ROS production and to the fact that there is no hyperoxic exposure occurring under this condition. Coupled with the results in the air and oxygen groups in which cells are indeed exposed to hyperoxia during the compressive phase, these findings suggest that decompression from hyperbaric exposure alone does not provoke the cellular response and that the gas exposure, including oxygen concentration during the compressive phase, influences the degree of injury manifest as respiratory dysfunction. This also is evident in the mitochondrial dynamics results discussed below, and influences the efficacy of the therapeutic approach we have investigated.

We delivered the first-generation cell-permeable succinate prodrug NV118, one of a series of *in vitro* test compounds, to cells as a potential means of preserving mitochondrial function otherwise disturbed by decompression from hyperbaric exposure. There is currently a large unmet need for evidence-based treatment related to diving injuries (Distelmaier et al., 2017) as well as a general need for mitochondrial therapies. In both the air and oxygen groups, the prophylactic use of NV118 resulted in increased basal respiration and decreased SRC. In the nitrogen group, there was no change the basal respiration but a significant increase in the SRC was present with NV118 administration. The potential value of NV118 in the setting of decompression injury is also reflected in the significant decrease in superoxide production in the air and the oxygen groups when compared to the untreated cells. There was a small but significant increase in superoxide production in the nitrogen group with NV118 treatment, but it did not exceed baseline values. The significance of this is unclear in light of the increased SRC without any appreciable change in other respiration parameters resulting as a response to NV118. It is clear, however, that select conditions of decompression from hyperbaric exposure, particularly decompression from hyperbaric air and oxygen exposure, impose a significant cellular response resulting in a decrease in SRC that may be explained in part as a result of excessive superoxide production. However, the correlation between SRC and ROS does not indicate a causal relationship; this requires further investigation. However, supplying the mitochondria with a substrate that bypasses CI provides additional support of aerobic metabolism for ATP generation (Ehinger et al., 2016).

The measurement of mitochondrial membrane potential further demonstrated that HAoSMCs subjected to decompression from hyperbaric exposure were injured because there was loss of TMRM signal observed. In particular, there was a significant decrease in the TMRM signal in both the perinuclear and peripheral regions of cells in the untreated decompression groups, which partially explains the changes in ATP-linked respiration and SRC along with altered superoxide production. The diminution of signal in the cell periphery may also serve as a biomarker of loss of bioenergetic capacity for cell function occurring in the cytosol. Likewise the reduction of mitochondrial potential in the perinuclear zone may be an integral component of nuclear-to-cytosol signaling that results in mobilization of mitochondrial resources in order to maintain ATP-based energy delivery the nucleus. This can potentially involve mitochondrial motility as is discussed below, which we have observed via imaging and image analysis to change in response to decompression from hyperbaric exposure. Our demonstration that pretreatment with NV118 improves mitochondrial membrane potential for all conditions/locations except for the cell periphery with nitrogen exposure supports the role of maintaining adequate mitochondrial membrane potential to generate ATP as exhibited in the improvement in ATP-linked and SRC respiration.

The measurements of mitochondrial dynamics, and in particular mitochondrial motility in both the perinuclear region and the cell periphery, which we have made following decompression from cell exposure to hyperbaric conditions, demonstrate that mitochondrial movement becomes enhanced. Coupled with the changes in respiration parameters and the concomitant reductions in mitochondrial potential, this indicates that mitochondria respond to a disequilibrium between cellular bioenergy needs and reduced bioenergetic capacity arising as a result of the exposure conditions. While the specific signaling for this response remains unknown, the response includes increased spatial exploration by mitochondria to seek usable bioenergy substrate. If cells subjected to decompression from hyperbaric conditions are first incubated with NV118, the presence of additional substrate for CII results in a net decrease in motility of mitochondria back to, or below, baseline levels. Our ability to partition the cell into the perinuclear and peripheral zones allows us to combine the mitochondrial motility results with an overall parameter of cellular bioenergetic performance. The scaled fractional ATP-linked respiration (Figure 6C) is used to discern that the mitochondrial dynamics and respiratory functions are coupled to yield preservation of bioenergy delivery to the cell nucleus despite the applied exposure conditions to induce cell perturbation. In the case of the oxygen exposure, the fact that cell viability remains equal to baseline experiment levels suggests that the energy demand of the nucleus is still sufficiently met despite the measured decrease in the perinuclear component of this parameter. However, the changes in cell circularity suggest that within the cell periphery there is has been some form of injury that results in inability of the cell to maintain shape. Again, the addition of NV118 shields the cells to a significant degree from these quantifiable changes, demonstrating that the cell-permeable succinate prodrug NV118 has positive effects in both the cell periphery and in the perinuclear region to protect cells from injury wrought by decompression from hyperbaric and hyperoxic exposure.

An important aspect of this work is our demonstration that decompression from hyperbaric and hyperoxic exposure are environmental factors that impair mitochondrial function in

HAoSMCs. Furthermore, we have shown that NV118 mitigates the mitochondrial dysfunction induced by these environmental factors to a degree sufficient to maintain or preserve many of the functional measures examined at, or closer to, baseline levels. Our results suggest that employing these experimental methods can be used to aid in identifying signaling- or pathway-dependent approaches to provide prophylaxis for toxicant-induced mitochondrial dysfunction, which may progress in the future to clinical utilization. This work can be generalized to address applications involving drug or environmental toxicants that cause quantifiable aberrations in bioenergy availability between the cell nucleus and periphery as a component of mitochondrial dysfunction and to pursuit of novel approaches of maintaining adequacy of intracellular bioenergy supply.

4. MATERIALS AND METHODS

4.1 EXPERIMENTAL MODEL DETAILS

4.1.1 Cell Culture—Adult primary human aortic smooth muscle cells (HAoSMCS) between passages one and eight were cultured in Vascular Cell Basal media (ATCC) without gentamicin. A 24-well polystyrene Seahorse XF cell culture plate was seeded at a density of 60,000 cells/100 μL 24 hours prior to mitochondria respiration assay experiments. For experiments to measure mitochondrial dynamics with fluorescence microscopy, cells were plated at a density of 10,000 cells per dish on fibronectin-coated MatTek 35-mm glass-bottom dishes approximately 48 hours before motility experiments. MatTek dishes were coated with 10 μg/ml fibronectin-PBS solution for 30 minutes prior to plating.

4.2 METHOD DETAILS

4.2.1 Decompression from Hyperbaric Exposure Conditions—In addition to baseline (ambient atmosphere) conditions, HAoSMCs were subjected to three distinct conditions of decompression from hyperbaric exposure to: (1) air; (2) nitrogen; and (3) oxygen based gas compositions defined below. Except for the baseline group, all hyperbaric exposures were performed at room temperature and under a pressure of 4.8 atmosphere (atm) added to atmospheric (ATA) for one hour. The hyperbaric exposure protocol was performed by first implementing a five-minute compression phase conducted at a rate of approximately one atm per minute, followed by the one-hour constant pressure phase at 4.8 atm ATA, and concluding the decompression phase back to ambient pressure occurring over five minutes, also at a rate of approximately one atm per min. All described hyperbaric exposures and decompressions were performed in a Nat'L BD model portable hyperbaric chamber rated for 100 PSI. Cells in the air exposure group were exposed to 19.8% O_2, 79.2% N_2 and 1.0% CO_2; cells in the nitrogen exposure group were exposed to 4.0% O_2, 95.0% N_2 and 1.0% CO_2; and those in the oxygen exposure group were exposed to 84.0% O_2, 15.0% N_2 and 1.0% CO_2. During hyperbaric exposures these gas mixtures yield the equivalent of 5.8% CO_2 as in (Jang et al., 2018c). Cells in the baseline group did not undergo hyperbaric exposure and subsequent decompression, however they were kept in the hyperbaric chamber at ambient pressure for one hour as in (Jang et al., 2018c). See Supplemental Figure 1 for data regarding stability of the baseline conditions.

4.2.2 Determination of Mitochondrial Respiration—Prior to the measurement of cellular respiration, cells were subjected to decompression from the hyperbaric exposure conditions described above. As in (Jang et al., 2018c), mitochondrial oxygen consumption rates (OCR) in pmol/min were evaluated in HAoSMC using the Seahorse XFe24 Analyzer (Agilent, Santa Clara, CA). The experiments were performed with unbuffered DMEM XF assay media supplemented with 2 mM GlutaMAX, 1 mM sodium pyruvate, and 5 mM glucose (pH 7.4 At 37 °C). Once calibration of the instrument was completed, select compounds were injected to obtain various respiratory states: (1) Basal respiration; (2) LEAK; (3) Maximum respiration (Max); and (4) Residual oxygen consumption (ROX). Basal respiration representing steady state energy turnover and ATP production was obtained first. Following measurement of basal respiration, oligomycin (2 μM) was injected to inhibit ATP synthase (Complex V or CV) to obtain LEAK. After obtaining the LEAK state, CCCP (1 μM) was injected to induce uncoupling that provides the maximum respiration (Max) of the cell. Finally, rotenone (0.5 μM) followed by antimycin A (0.5 μM) was injected in order to inhibit all mitochondrial respiration. This provides ROX that is an assessment of non-mitochondrial oxygen consumption. We obtained two other states, ATP-linked respiration and spare respiratory capacity or SRC. ATP-linked respiration is oxygen consumption related to the production of ATP at Complex V. It is calculated as basal respiration minus LEAK after the injection of oligomycin to inhibit Complex V. SRC is a measure of mitochondrial reserve available for cells to produce ATP in response to conditions which induce increase in metabolic demand. It is calculated as maximal respiration minus basal respiration. Basal, LEAK and Max respiration were each corrected for ROX to provide mitochondrial respiration. All respiratory states described above were measured at three consecutive time points. These three values were averaged to give a single measure of respiration for each state for each cell culture well. After each Seahorse run, metabolic activity in each well was determined by relative fluorescence measurements made in a Synergy H1 plate reader (BioTek, Winooski, VT, USA). Cells in each well were stained with 100 nM Calcein-AM for 30 minutes prior to imaging. Seahorse data were then normalized using metabolic activity; background readings for each plate were calculated by averaging the OCRs from the background wells for those plates and subtracted from all subsequent readings. Erratic or extreme background well readings were excluded. All experiments were repeated in triplicate in runs performed on at least separate days. Each well was analyzed individually, and the resultant data are presented as the mean ± standard error on mean (SEM) for all experiments.

As occurred in (Jang et al., 2018a), the Oxygen group showed consistently negative values of respiratory states due to the Seahorse XF cell culture plate absorbing oxygen under high pressure in the hyperbaric chamber resulting in unreliable negative OCR values. Based on our previous modified approach for this group, we performed the hyperbaric exposure to oxygen and subsequent decompression using a fully confluent T75 cell culture plate (Resseguie et al., 2015). After the decompression was completed, cells were washed with PBS and detached using 0.25% trypsin. The detached cells were then plated on Cell-Tak coated 24-well PS Seahorse XF plates at a density of 60,000 cells/100 μL. The plated Seahorse XF plate was centrifuged for 1 minute to ensure proper cell adherence to Cell-Tak before the plate was loaded into the XF^{e}24 Analyzer. The time between the end of

hyperbaric exposure and decompression and start of the mitochondrial respiration assay was approximately 30 min. A set of preliminary of experiments comparing OCR values following decompression from hyperbaric exposure to air obtained using this modified technique and the standard approach demonstrated no significant differences in the measurements. This provided reassurance that the OCR measurements performed with hyperbaric oxygen are valid.

In addition, a succinate-based experimental compound, NV101-118 (NV118, diacetoxy-methyl succinate, Isomerase Therapeutics Ltd.) at a final concentration of 500 μM was used in this study. 1M NV118 previously reconstituted in DMSO was further diluted in unbuffered XF media for use in the XF^e24 Analyzer. Hence, unbuffered XF media was also used as vehicle for XF^e experiments. The stock (100%) DMSO concentration was 14.079 M. Microscopy experiments with NV118 were done at 25 μM. This concentration was chosen after separate experiments showed higher doses of NV118 had an inhibitory effect similar to the cell-permeable complex II inhibitor NV161 at similar concentrations.

4.2.3 Determination of Mitochondrial Dynamics—In addition to the obtained mitochondrial respiration in all conditions, we also measured mitochondrial dynamics in all decompression from hyperbaric exposure conditions. Mitochondrial dynamics measurements included determination of (1) Net mitochondrial movement; (2) Mitochondrial number; and (3) Mitochondrial size. These were subdivided into two intracellular zone based measurements as described below. First we obtained whole cell mitochondrial dynamics data for measurements using wide-field fluorescence microscopy as described in specific detail in our previous work (Barel et al., 2017; Eckmann et al., 2019; Jang et al., 2019a; Jang et al., 2018c; Jang et al., 2017c; Kandel et al., 2015). The day before experiments, cells were transfected with CellLight Mitochondria-GFP, BacMam 2.0 (Life Technologies, Grand Island, NY, USA) at a concentration of 40 particles/cell, and kept in the dark at 37°C. Cells were also stained with DAPI and were placed in Recording HBSS (HBSS pH 7.4 with 1.3 mM $CaCl_2$, 0.9 mM $MgCl_2$, 2 mM glutamine, 0.1 g/L heparin, 5.6 mM glucose, and 1% FBS) for imaging. Cells were imaged using an Olympus IX-51 inverted epifluorescence microscope with an Olympus 40x oil immersion objective lens, a Hamamatsu ORCA camera (2048 X 2048 pixels) with an LED light source from Lumencor. Images were collected using Metamorph 10.7.8.9 software. For each motility experiment, cells were visualized using a standard FITC filter, and isolated cells with well-resolved mitochondria were selected. Following exposure to experimental conditions, cells were imaged every 3 seconds for a total of 5 minutes, giving 101 image frames which were dubbed “whole cell” frames.

Image pre-processing and image analysis of whole cell motility included the use of ImageJ and MATLAB following established methodology (Eckmann et al., 2019; Jang et al., 2017c; Kandel et al., 2015). Obtained DAPI images (maintaining field of view) were thresholded on ImageJ and our in-house written MATLAB program was used to detect the edge pixels and centroid of the cell nucleus. Straight lines were then constructed radially from the centroid to each of the edge pixels and their angles, measured. Using the Pythogorean theorem, the line created was then extended by a fixed distance of 20 pixels (3.2 um, (Eckmann et al., 2019)) with its angle maintained and repeated for all end pixel points to generate new end pixel

points which were connected to form a continuous border (see Figure 1B-E). The space between the border of the cell nucleus and this second continuous border was dubbed the "perinuclear zone". This zone was subtracted from each of the "whole cell" frames to provide corresponding new frames dubbed the "peripheral zone". Two sets of folders (perinuclear zone, and peripheral zone) were then analyzed using an additional in-house written MATLAB program for mitochondrial motility in which time-lapse images were convolved using the 5×5 edge-detection filter (Kandel et al., 2015). Then, images were converted to the frequency domain using a Fast Fourier Transform (FFT) in ImageJ, and subjected to a bandpass filter ranging from 2 pixels (~0.3 μm with our resolution) to 100 pixels (~16 μm). The MATLAB algorithm reads the current frame and the built-in function bwconncomp is used to find the connected white objects in the image which allows us to quantify both mitochondrial movement and mitochondrial dimensions. All of the scripts and instructions of these algorithm are readily available online for public use, with the expectation of proper citation, at www.github.com/kandelj/MitoSPT.

Cells were analyzed individually using these imaging techniques. All conditions were repeated at least three times from different days and the analysis was performed on resulting videos from all trials for each condition. The findings for all cells across all trials were then pooled for each condition, as in (Kandel et al., 2015), with 14-17 cells per group.

4.2.4 Determination of Superoxide Production and Mitochondrial Inner Membrane Potential—

Measurement of superoxide production and mitochondrial inner membrane potential were conducted in separate experiments performed in triplicate on separate days. To assess superoxide production, on the day of each experiment, cells were incubated with Red Mitochondrial Superoxide Indicator (MitoSOX) working solution at 5 μM for 10 minutes at 37 °C, protected from light, washed with warm Recording HBSS and then mounted in warm Recording HBSS for imaging. Fluorescence intensity in individual cells (at least 16 per group) was measured with ImageJ software and Corrected Total Cell Fluorescence (CTCF) was calculated through the formula (CTCF = Integrated Density – Area of Cell × Background Fluorescence).

In another batch of experiments, mitochondrial membrane potential was obtained using TMRM. On the day of each experiment, cells were incubated with DAPI and with TMRM in 20 nM working solution for 30 minutes in the dark at 37 °C. Cells were rinsed twice and then mounted in Recording HBSS for imaging. To obtain a zone around the nucleus that would separate the perinuclear and peripheral regions, images with TMRM and DAPI stains were merged on ImageJ and a line was traced around the nucleus at a distance of 20 pixels or (3.2 μm) from the nuclear edge. This tracing was saved onto the ROI manager (on ImageJ). The TMRM frame was then duplicated; the first of which was thresholded using the same method for preprocessing motility images after which the mitochondria in the image were isolated using the Create Selection function (creates a region of interest surrounding thresholded objects, essentially isolating individual mitochondria) and then saved onto the ROI manager. These ROIs were then superimposed on the duplicate TMRM frame. Using the line tracing zone saved onto the ROI manager, the perinuclear and peripheral zones were separated out. Once separated, using the Measure function on ImageJ, average fluorescence measurements in the ROIs (minimum 10 per region per cell) were

recorded. For both the perinuclear and peripheral zones, background measurements were also made (using the Measure function) near mitochondria located in their respective zones. The final membrane potential value measured is the average background intensity subtracted from the average pixel intensity of mitochondria derived from the ROIs. An additional control experiment was performed with cells under baseline conditions with 10 μM CCCP added in order to collapse the mitochondrial membrane potential. Membrane potential experiments were performed on at least three separate days with a minimum of 16 cells per group.

4.2.5 Scaled Fractional ATP-Linked Respiration—Following the method we established in (Eckmann et al., 2019), we used the various data obtained to construct the fractional intracellular perinuclear and peripheral components of the regional distribution of bioenergetic capacity. By combining our determination of mitochondrial number, the dimensions of mitochondria and the fraction of mitochondria distributed within the perinuclear and peripheral domains, we directly construct of the net mitochondrial volume fraction present in each domain. Based on (Lionetti et al., 1996) we applied a linearized relationship between mitochondrial potential and cellular respiration rate to the domain-specific measurement of mitochondrial potential in each of the perinuclear and peripheral regions. Using the results for mitochondrial volume fraction distribution permitted calculation of the perinuclear and the peripheral fractional contributions to total cellular respiration. We applied the values which were determined for ATP-linked respiration and thus established the fractional intracellular perinuclear and peripheral contributions as the regional distribution of bioenergetic capacity (Eckmann et al., 2019).

4.2.6 Cell Cytoskeletal Imaging—In a separate cohort of experiments conducted on at least 3 separate days to evaluate the effect of decompression on actin, cells were transfected with CellLight Actin-RFP, BacMam 2.0 and placed in Recording HBSS the day prior to experiments. To evaluate the effect of decompression from hyperbaric exposure on microtubules, cells were incubated in 250 nM Tubulin Tracker Green (Life Technologies) for 30 min at 37 °C prior to being subjected to identical hyperbaric and decompression conditions. Hoechst (20 mM) was also used to stain the nucleus in the cytoskeletal imaging experiments. Cell were imaged at 40X with an oil immersion objective lens through a Cy3 filter and the resulting images were then pseudocolored using Image J software.

4.2.7 Cell Circularity—ImageJ was used to quantify the circularity of cells to determine if experimental conditions had any effect on cell morphology. Cell circularity, C, was measured on a scale of 0 to 1 from least to most circular after first creating a mask of each cell. Image analysis was then used to determine $C = 4\pi A/P^2$, in which A = cell area and P = cell perimeter ($C = 1$ for spherical cells; $C < 1$ for cells deformed from circular cross section is energy requiring) with 16 cells per group being evaluated. The circularity parameter measures the cell's ability to maintain shape and relies on multiple factors, including energy dependent processes to preserve cytoskeletal integrity. Alterations in cell circularity are a measure of change in stress fiber response to many inputs, including mitochondrial function and its influence on maintenance of cell membrane pinning (Kandel et al., 2017).

4.3 QUANTIFICATION AND STATISTICAL ANALYSIS

Data are presented as mean ± S.E.M., if not indicated otherwise. Graph Pad Prism 8.0 was used for statistical analysis. Sigmaplot 14.0 was used for data presentation. Data were tested for normal distribution with the D'Agostino and Pearson omnibus normality test. Differences between groups were assessed using ANOVA in repeated measures. Post-hoc pair wise comparisons using Tukey Kramer t-tests to adjust for multiple comparisons were used to assess differences between groups and respiratory states. A P value of < 0.05 was considered statistically significant. Statistical parameters can be found in figure legends.

Supplementary Material

Refer to Web version on PubMed Central for supplementary material.

Acknowledgments

This work was funded by grant N000141712643 from the Office of Naval Research (D.M.E.) and grant K08HL136858 from the National Heart, Lung, and Blood Institute (D.H.J.).

7. References

Barel O, Malicdan MC, Ben-Zeev B, Pri-Chen H, Stephen J, Castro IG, Metz J, Atawa O, Moshkovitz S, Ganelin E, et al. (2017). Stuck on the tracks: Deleterious mutations in TRAK1 cause severe fatal encephalopathy with cerebral inclusion bodies. Brain 140, 568–581. [PubMed: 28364549]

Chacko BK, Kramer PA, Ravi S, Benavides GA, Mitchell T, Dranka BP, Ferrick D, Singal AK, Ballinger SW, Bailey SM, et al. (2014). The Bioenergetic Health Index: a new concept in mitochondrial translational research. Clinical science (London, England : 1979) 127, 367–373.

Chandel NS (2014). Mitochondria as signaling organelles. BMC Biol 12.

Distelmaier F, Haack TB, Wortmann SB, Mayr JA, and Prokisch H (2017). Treatable mitochondrial diseases: cofactor metabolism and beyond. Brain 140, e11. [PubMed: 27993888]

Dzeja PP, Bortolon R, Perez-Terzic C, Holmuhamedov EL, and Terzic A (2002). Energetic communication between mitochondria and nucleus directed by catalyzed phosphotransfer. Proc Natl Acad Sci U S A 99, 10156–10161. [PubMed: 12119406]

Eckmann DM, Ranganathan A, Owiredu S, and Jang DH (2019). Compartmentalization of bioenergetic substrate delivery in intact cells. ASME Journal of Heat Transfer 141, 052001.

Ehinger JK, Piel S, Ford R, Karlsson M, Sjovall F, Frostner EA, Morota S, Taylor RW, Turnbull DM, Cornell C, et al. (2016). Cell-permeable succinate prodrugs bypass mitochondrial complex I deficiency. Nat Commun 7.

Galvan DL, Green NH, and Danesh FR (2017). The hallmarks of mitochondrial dysfunction in chronic kidney disease. Kidney Int 92, 1051–1057. [PubMed: 28893420]

Gorini S, De Angelis A, Berrino L, Malara N, Rosano G, and Ferraro E (2018). Chemotherapeutic Drugs and Mitochondrial Dysfunction: Focus on Doxorubicin, Trastuzumab, and Sunitinib. Oxid Med Cell Longev 2018, 7582730. [PubMed: 29743983]

Guigni BA, Callahan DM, Tourville TW, Miller MS, Fiske B, Voigt T, Korwin-Mihavics B, Anathy V, Dittus K, and Toth MJ (2018). Skeletal Muscle Atrophy and Dysfunction in Breast Cancer Patients: Role for Chemotherapy-Derived Oxidant Stress. Am J Physiol Cell Physiol 315, C744–C756. [PubMed: 30207784]

Hubley MJ, Moerland TS, and Rosanske RC (1995). Diffusion coefficients of atp and creatine phosphate in isolated muscle: pulsed gradient 31p nmr of small biological samples. NMR in Biomedicine 8, 72–78. [PubMed: 7547189]

Jang DH, Greenwood JC, Owiredu S, Ranganathan A, and Eckmann DM (2019a). Mitochondrial networking in human blood cells with application in acute care illnesses. Mitochondrion 44, 27–34. [PubMed: 29275149]

Jang DH, Greenwood JC, Spyres MB, and Eckmann DM (2017a). Measurement of Mitochondrial Respiration and Motility in Acute Care: Sepsis, Trauma, and Poisoning. J Intensive Care Med 32, 86–94. [PubMed: 27443317]

Jang DH, Kelly M, Hardy K, Lambert DS, Shofer FS, and Eckmann DM (2017b). A preliminary study in the alterations of mitochondrial respiration in patients with carbon monoxide poisoning measured in blood cells. Clin Toxicol 55, 579–584.

Jang DH, Khatri UG, Mudan A, Love JS, Owiredu S, and Eckmann DM (2018a). Translational application of measuring mitochondrial functions in blood cells obtained from patients with acute poisoning. J Med Toxicol 14, 144–151. [PubMed: 29536431]

Jang DH, Khatri UG, Shortal BP, Kelly M, Hardy K, Lambert DS, and Eckmann DM (2018b). Alterations in mitochondrial respiration and reactive oxygen species in patients poisoned with carbon monoxide treated with hyperbaric oxygen. Intensive Care Med Exp 6, 4. [PubMed: 29383459]

Jang DH, Orloski CJ, Owiredu S, Shofer FS, Greenwood JC, and Eckmann DM (2019b). Alterations in mitochondrial function in blood cells obtained from patients with sepsis presenting to an emergency department. Shock 51, 580–584. [PubMed: 29905672]

Jang DH, Owiredu S, Ranganathan A, and Eckmann DM (2018c). Acute decompression following simulated dive conditions alters mitochondrial respiration and motility. Am J Physiol Cell Physiol 315, C699–C705. [PubMed: 30110561]

Jang DH, Seeger SC, Grady ME, Shofer FS, and Eckmann DM (2017c). Mitochondrial dynamics and respiration within cells with increased open pore cytoskeletal meshes. Biol Open 6, 1831–1839. [PubMed: 29109116]

Kandel J, Angelin AA, Wallace DC, and Eckmann DM (2016). Mitochondrial respiration is sensitive to cytoarchitectural breakdown. Integrative Biology 8, 1170–1182. [PubMed: 27734042]

Kandel J, Chou P, and Eckmann DM (2015). Automated detection of whole-cell mitochondrial motility and its dependence on cytoarchitectural integrity. Biotechnol. Bioeng 112, 1395–1405. [PubMed: 25678368]

Kandel J, Picard M, Wallace DC, and Eckmann DM (2017). Progressive increase in mtDNA 3243A>G heteroplasmy is associated with nonlinear alterations in cytoskeletal protein expression and cell mechanics. Journal of the Royal Society Interface 14, 20170071.

Kim Y, Vadodaria KC, Lenkei Z, Kato T, Gage FH, Marchetto MC, and Santos R (2019). Mitochondria, Metabolism, and Redox Mechanisms in Psychiatric Disorders. Antioxid Redox Signal *In Press.*

Kotiadis VN, Duchen MR, and Osellame LD (2014). Mitochondrial quality control and communications with the nucleus are important in maintaining mitochondrial function and cell health. Biochim Biophys Acta 1840, 1254–1265. [PubMed: 24211250]

Kucera O, Endlicher R, Rychtrmoc D, Lotkova H, Sobotka O, and Cervinkova Z (2017). Acetaminophen toxicity in rat and mouse hepatocytes in vitro. Drug Chem Toxicol 40, 448–456. [PubMed: 27960556]

Lee HK, Cho YM, Kwak SH, Lim S, Park KS, and Shim EB (2010). Mitochondrial dysfunction and metabolic syndrome-looking for environmental factors. Biochim Biophys Acta 1800, 282–289. [PubMed: 19914351]

Leitch DR, and Hallenbeck JM (1985). Electrocardiographic changes in serious decompression sickness. Aviat Space Env Med 56, 966–971. [PubMed: 4062771]

Lin H, Stankov MV, Hegermann J, Budida R, Panayotova-Dimitrova D, Schmidt RE, and Behrens GMN (2019). Zidovudine-mediated autophagy inhibition enhances mitochondrial toxicity in muscle cells. Antimicrob Agents Chemother 63, e01443–01418. [PubMed: 30373793]

Lionetti L, Iossa S, Brand MD, and Liverini G (1996). Relationship between membrane potential and respiration rate in isolated liver mitochondria from rats fed an energy dense diet. Mol Cell Biochem 158, 133–138. [PubMed: 8817475]

Mazur A, Lambrechts K, Wang Q, Belhomme M, Theron M, Buzzacott P, and Guerrero F (2016). Influence of decompression sickness on vasocontraction of isolated rat vessels. J Appl Physiol (1985) 120, 784–791. [PubMed: 26769950]

Meyer JN, Leung MC, Rooney JP, Sendoel A, Hengartner MO, Kisby GE, and Bess AS (2013). Mitochondria as a target of environmental toxicants. Toxicol Sci 134, 1–17. [PubMed: 23629515]

Piel S, Ehinger JK, Chamkha I, Frostner EA, Sjovall F, Elmer E, and Hansson MJ (2018). Bioenergetic bypass using cell-permeable succinate, but not methylene blue, attenuates metformin-induced lactate production. Intensive Care Med Exp 6, 22. [PubMed: 30069806]

Porporato PE, Filigheddu N, Pedro JMB, Kroemer G, and Galluzzi L (2018). Mitochondrial metabolism and cancer. Cell Res 28, 265–280. [PubMed: 29219147]

Ramachandran R, and Wierzbicki AS (2017). Statins, Muscle Disease and Mitochondria. J Clin Med 6, 75.

Rangamani P, Xiong G, and Iyengar R (2014). Multiscale Modeling of Cell Shape from the Actin Cytoskeleton In Progress in Molecular Biology and Translational Science. Blackwell KT, ed. (Academic Press), pp. 143–167.

Resseguie EA, Staversky RJ, Brookes PS, and O'Reilly MA (2015). Hyperoxia activates ATM independent from mitochondrial ROS and dysfunction. Redox biology 5, 176–185. [PubMed: 25967673]

Vann RD, Butler FK, Mitchell SJ, and Moon RE (2011). Decompression illness. Lancet 377, 153–164. [PubMed: 21215883]

Wang Q, Guerrerok F, Mazur A, Lambrechts K, Buzzacott P, Belhomme M, and Theron M (2015). Reactive oxygen species, mitochondria, and endothelial cell death during in vitro simulated dives. Medicine & Science in Sports & Exercise 47.

Whelan SP, and Zuckerbraun BS (2013). Mitochondrial signaling: forwards, backwards, and in between. Oxid Med Cell Longev 2013, 351613. [PubMed: 23819011]

Wilkins HM, and Swerdlow RH (2016). Relationships Between Mitochondria and Neuroinflammation: Implications for Alzheimer's Disease. Curr Top Med Chem 16, 849–857. [PubMed: 26311426]

Highlights

- Vascular smooth muscle cells are decompressed from hyperbaric exposure
- Mitochondrial motility and respiratory function are affected.
- A succinate prodrug provides partial prophylaxis from these effects

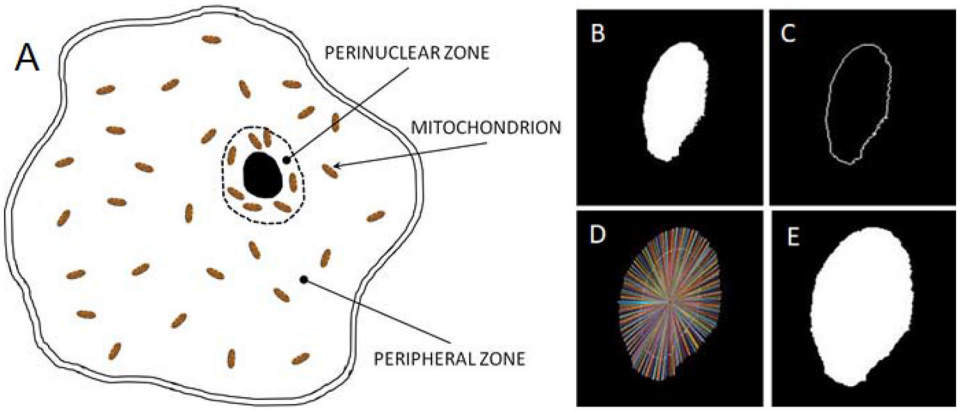

Figure 1. Intracellular partitioning of mitochondria into perinuclear and peripheral zones.

(A) Schematic of intracellular partitioning of mitochondria into perinuclear and peripheral regions. Cell image analysis steps (see Methods Section) demonstrating creation of mask for the cell nucleus (B) and its edge (C) from which a discrete perinuclear border region is determined (D) and a new mask of the nucleus plus the perinuclear zone is created (E).

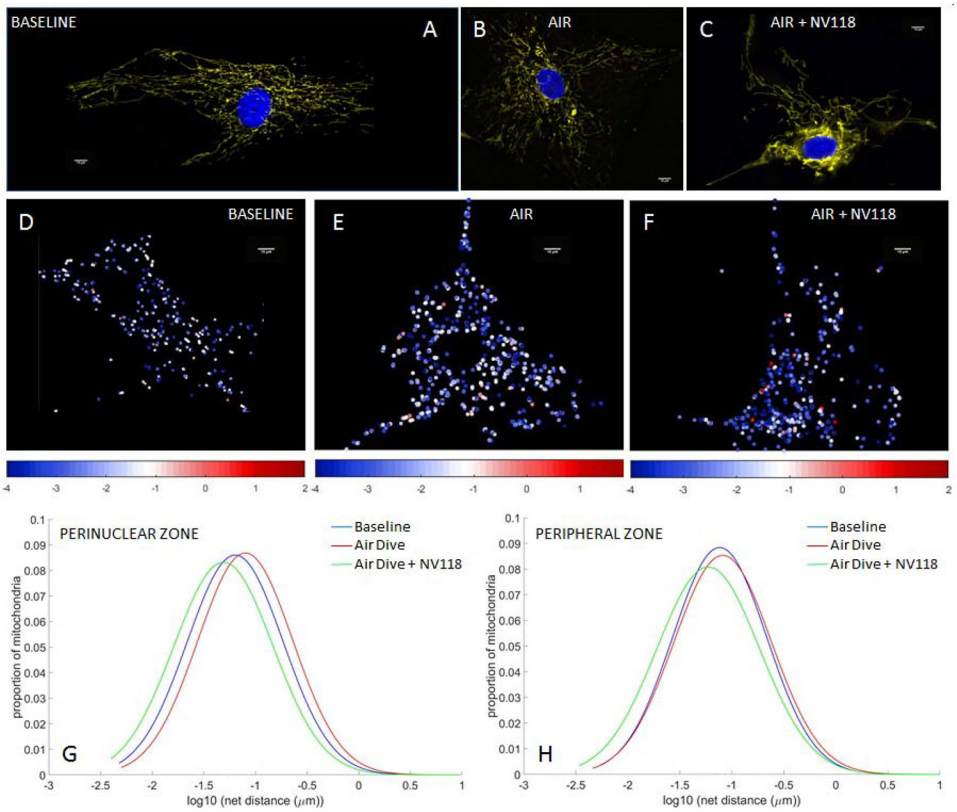

Figure 2. Alterations in mitochondrial potential and motility following decompression from hyperbaric air exposure are partially prevented by NV118 administration.

Tetramethylrhodamine, methyl ester (TMRM) fluorescence images of mitochondrial intermembrane potential in human aortic smooth muscle cells (HAoSMCs) (A) at baseline, (B) following decompression from hyperbaric air and (C) and with NV118 added prior to decompression from hyperbaric air. Cell nuclei are identified via DAPI fluorescence and appear blue. (D-F) Heat maps of individual mitochondrial net movement at baseline (D), following decompression from hyperbaric air (E) and following decompression from hyperbaric air with NV118 pretreatment (F). Each dot represents a distinct mitochondrion in its final location after tracking, and each dot's color represents the log of the net distance traveled according to the color bar beneath the image. All size bars are 10 μm. (G,H) Lognormal distribution of net distances traveled by all mitochondria at baseline, following decompression from hyperbaric air and following decompression from hyperbaric air with NV118 pretreatment groups in the perinuclear and peripheral zone, respectively.

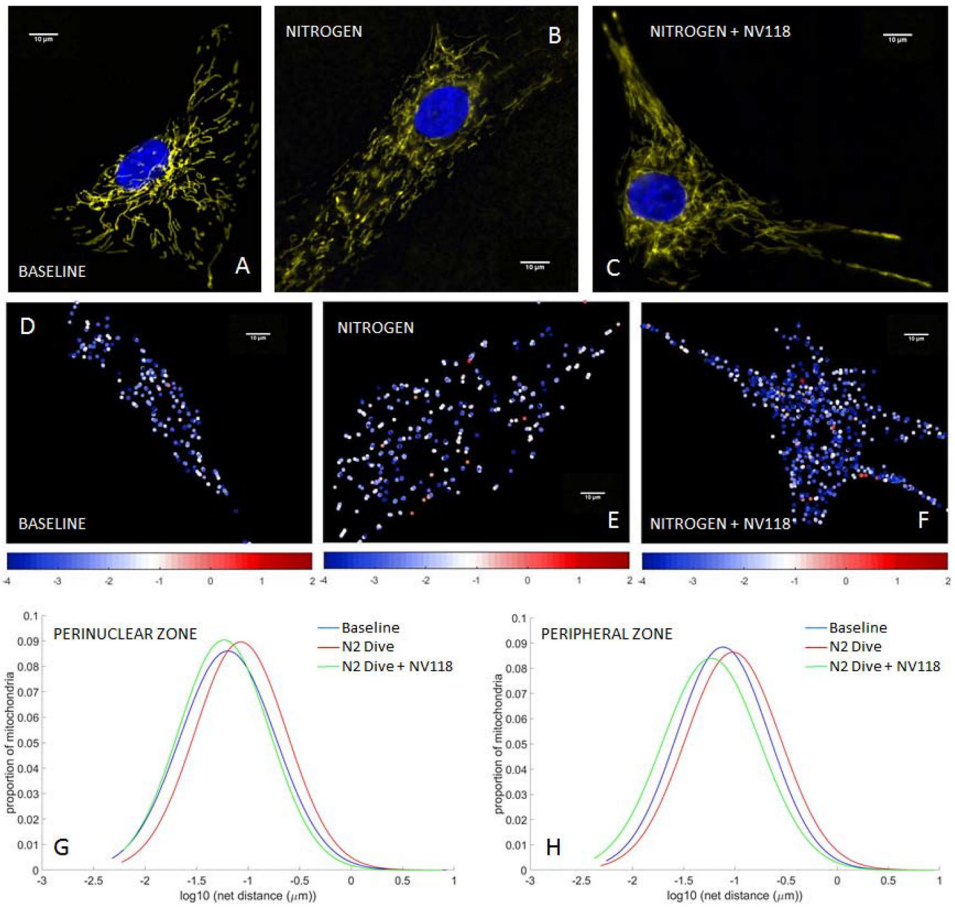

Figure 3. Alterations in mitochondrial potential and motility following decompression from hyperbaric nitrogen exposure are partially prevented by NV118 administration.

Tetramethylrhodamine, methyl ester (TMRM) fluorescence images of mitochondrial intermembrane potential in human aortic smooth muscle cells (HAoSMCs) (A) at baseline, (B) following decompression from hyperbaric nitrogen and (C) and with NV118 added prior to decompression from hyperbaric nitrogen. Cell nuclei are identified via DAPI fluorescence and appear blue. (D-F) Heat maps of individual mitochondrial net movement at baseline (D), following decompression from hyperbaric nitrogen (E) and following decompression from hyperbaric nitrogen with NV118 pretreatment (F). Each dot represents a distinct mitochondrion in its final location after tracking, and each dot's color represents the log of the net distance traveled according to the color bar beneath the image. All size bars are 10 μm. (G,H) Lognormal distribution of net distances traveled by all mitochondria at baseline, following decompression from hyperbaric nitrogen and following decompression from hyperbaric nitrogen with NV118 pretreatment groups in the perinuclear and peripheral zone, respectively.

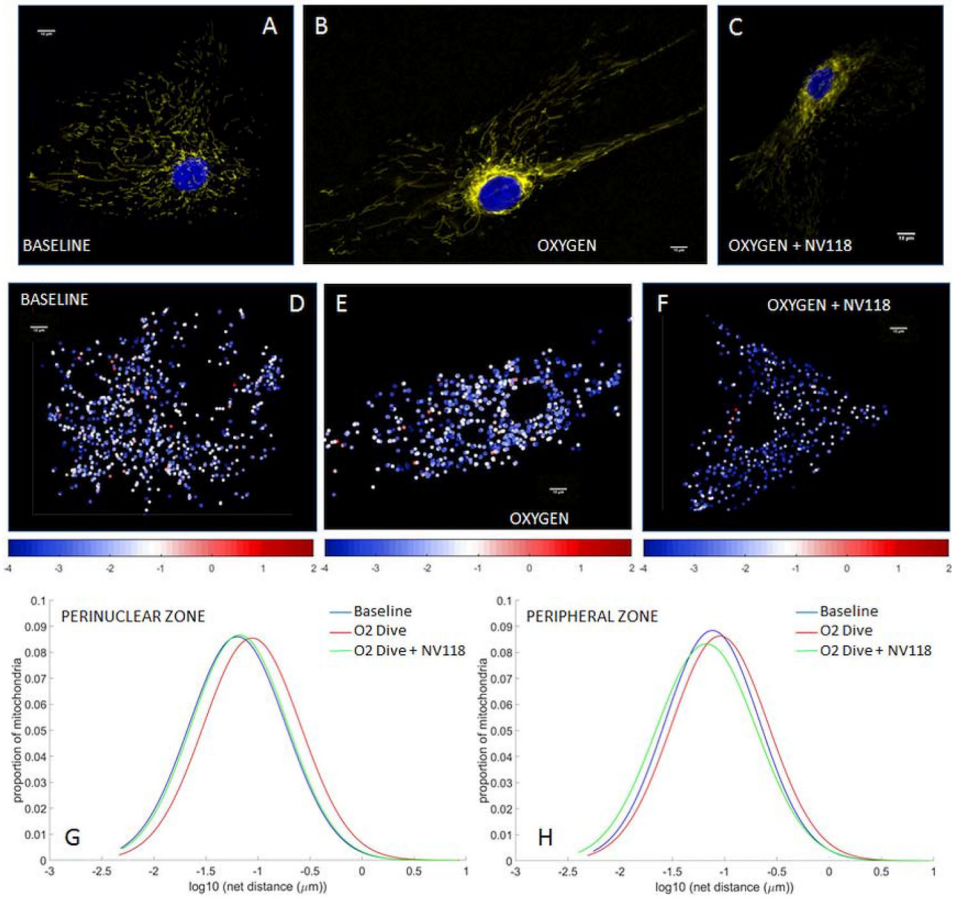

Figure 4. Alterations in mitochondrial potential and motility following decompression from hyperbaric oxygen exposure are partially prevented by NV118 administration.

Tetramethylrhodamine, methyl ester (TMRM) fluorescence images of mitochondrial intermembrane potential in human aortic smooth muscle cells (HAoSMCs) (A) at baseline, (B) following decompression from hyperbaric oxygen and (C) and with NV118 added prior to decompression from hyperbaric oxygen. Cell nuclei are identified via DAPI fluorescence and appear blue. (D-F) Heat maps of individual mitochondrial net movement at baseline (D), following decompression from hyperbaric oxygen (E) and following decompression from hyperbaric oxygen with NV118 pretreatment (F). Each dot represents a distinct mitochondrion in its final location after tracking, and each dot's color represents the log of the net distance traveled according to the color bar beneath the image. All size bars are 10 μm. (G,H) Lognormal distribution of net distances traveled by all mitochondria at baseline, following decompression from hyperbaric oxygen and following decompression from hyperbaric oxygen with NV118 pretreatment groups in the perinuclear and peripheral zone, respectively.

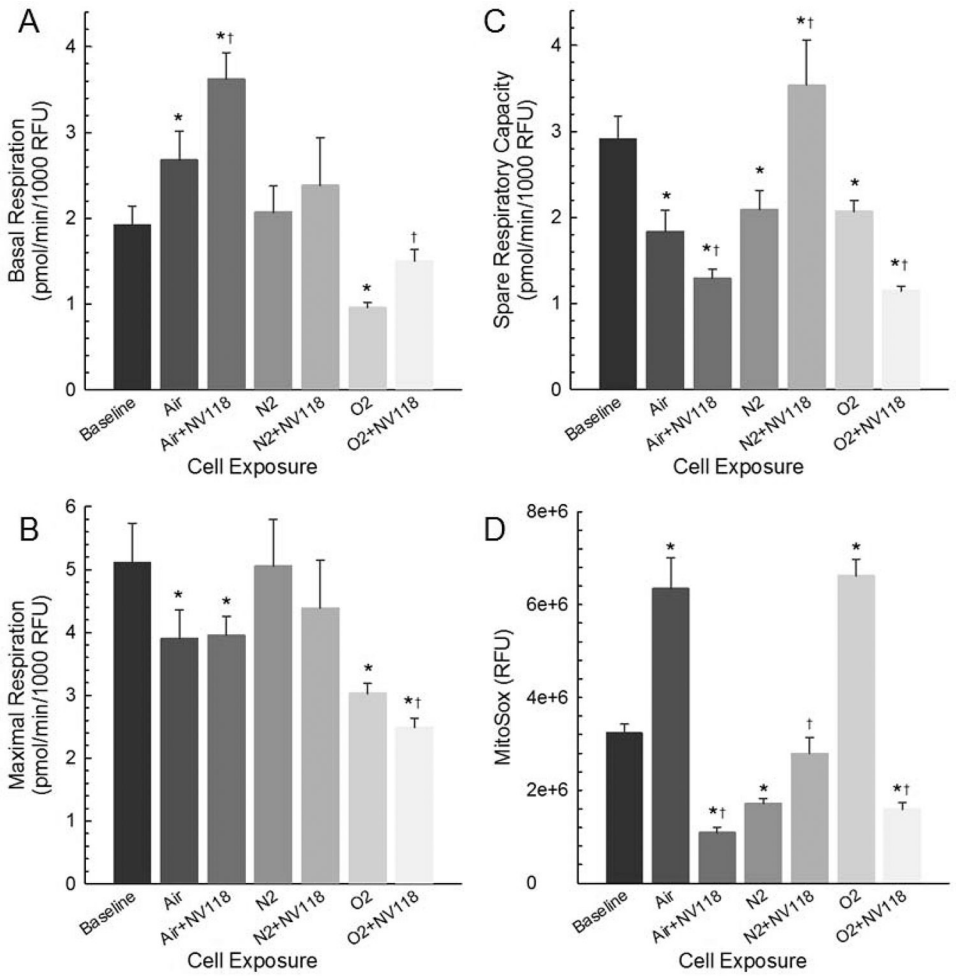

Figure 5. Key cellular respiration parameters are sensitive to decompression and cell-permeable succinate prodrug NV118.

(A) Basal cellular respiration, (B) Maximal cellular respiration, (C) Spare Respiratory Capacity and (D) MitoSox-based fluorescence indicating superoxide production in HAoSMCs at baseline, following decompression from hyperbaric exposure conditions and with NV118 added prior to decompression from hyperbaric exposure conditions. Data are represented as mean ± SEM. * $p < 0.05$ compared to baseline; † $p < 0.05$ compared to same cell exposure without NV118 pretreatment.

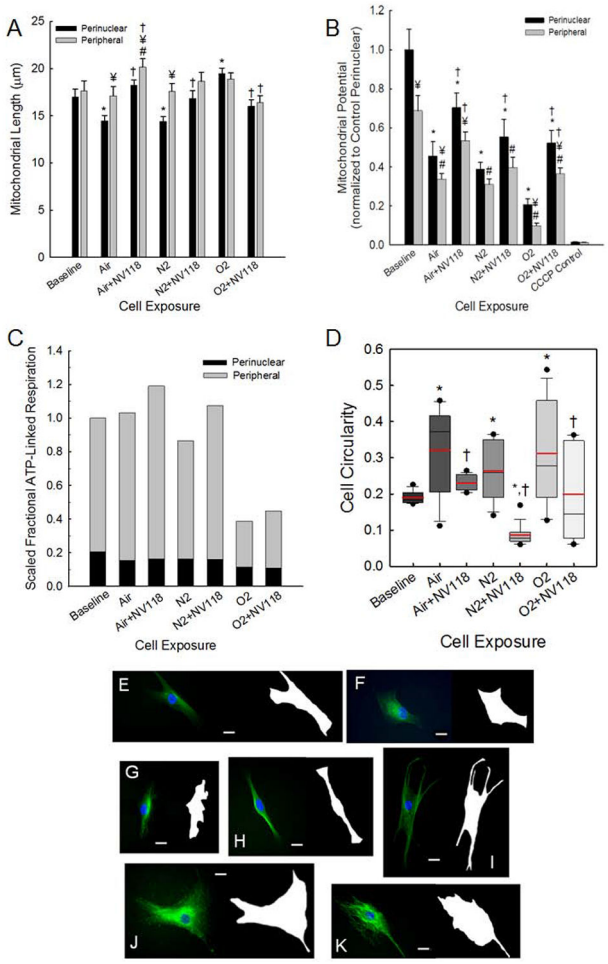

Figure 6. Intracellular mitochondrial partitioning reveals cell-permeable succinate prodrug NV118 partially preserves mitochondrial dynamics, respiration and nuclear bioenergetics following decompression from hyperbaric exposure.

Mitochondrial length (A) and intermembrane potential (B) in both the perinuclear and cell peripheral regions are indicated for HAoSMCs at baseline, following decompression from hyperbaric exposures and with NV118 added prior to hyperbaric exposure and decompression. Intermembrane potential following CCCP administration is shown as a control. Data are represented as mean ± SEM. * $p < 0.05$ compared to baseline, perinuclear region; # $p < 0.05$ compared to baseline, peripheral region; ¥ $p < 0.05$ compared to perinuclear region, same cell exposure; † $p < 0.05$ compared to same cell exposure without NV118 pretreatment. (C) Stacked bar graphs of scaled fractional ATP-linked respiration in the perinuclear and peripheral cell regions for HAoSMCs at baseline, following decompression from hyperbaric exposure and with NV118 added prior to decompression from hyperbaric exposure. (D) Box plots of cell circularity for each group, 16 cells per group. Solid circles appear at 5^{th} and 95^{th} percentiles, whiskers extend to 10^{th} and 90^{th} percentiles, boxes extend to the 25^{th} and 75^{th} percentiles, median values appear as a black line and mean values appear as a red line. * $p < 0.05$ compared to baseline; † $p < 0.05$ compared to same cell exposure without NV118 pretreatment. (E-K) Fluorescence images of tubulin stained cells with corresponding masks created for calculating circularity of cells.

Scale bar is set at 20 μm. Images are for baseline (E) and following decompression from hyperbaric exposure to air (F), air with NV118 pretreatment (G), nitrogen (H), nitrogen with NV118 pretreatment (I), oxygen (J), and oxygen with NV118 pretreatment (K).

Table 1.

Mean net distance traveled by mitochondria in cell perinuclear and peripheral regions and P values from comparisons between groups (14-17 cells per group).

Cell Region and Condition		Mean Net Distance (nm)	P Value			
			Baseline	Air	N_2	O_2
Perinuclear	Baseline	65.7366	--	--	--	--
	Air	88.4274	1.91E-13	--	--	--
	Air+NV118	49.903	6.48E-06	6.93E-18	--	--
	N_2	96.4737	4.28E-26	--	--	--
	N_2+NV118	66.6936	2.89E-02	--	7.42E-12	--
	O_2	90.6153	8.63E-21	--	--	--
	O_2+NV118	61.7904	7.13E-04	--	--	3.56E-10
Peripheral	Baseline	69.9495	--	--	--	--
	Air	86.7702	5.82E-07	--	--	--
	Air+NV118	55.903	1.68E-11	7.01E-46	--	--
	N_2	97.8861	2.15E-38	--	--	--
	N_2+NV118	70.98	8.49E-02	--	1.83E-53	--
	O_2	97.5637	6.57E-33	--	--	--
	O_2+NV118	67.363	9.22E-04	--	--	9.26E-75